

Topological Hall Effect Anisotropy in Kagome Bilayer Metal Fe₃Sn₂

Qianheng Du,^{1,2,*} Zhixiang Hu,^{1,2,*} Myung-Geun Han,¹ Fernando Camino^{1,3},, Yimei Zhu,¹ and C. Petrovic^{1,2,§}
¹*Condensed Matter Physics and Materials Science Department, Brookhaven National Laboratory, Upton, New York 11973, USA*
²*Department of Materials Science and Chemical Engineering, Stony Brook University, Stony Brook, New York 11790, USA*
³*Center for Functional Nanomaterials, Brookhaven National Laboratory, Upton, New York 11973, USA*

 (Received 9 March 2022; revised 7 July 2022; accepted 28 October 2022; published 30 November 2022)

Kagome lattice materials have attracted growing interest for their topological properties and flatbands in electronic structure. We present a comprehensive study on the anisotropy and out-of-plane electric transport in Fe₃Sn₂, a metal with bilayer of Fe kagome planes and with massive Dirac fermions that features high-temperature noncollinear magnetic structure and magnetic skyrmions. For the electrical current path along the *c* axis, in micron-size crystals, we found a large topological Hall effect over a wide temperature range down to spin-glass state. Twofold and fourfold angular magnetoresistance are observed for different magnetic phases, reflecting the competition of magnetic interactions and magnetic anisotropy in kagome lattice that preserve robust topological Hall effect for inter-kagome bilayer currents. This provides new insight into the anisotropy in Fe₃Sn₂, of interest in skyrmionic-bubble application-related micron-size devices.

DOI: [10.1103/PhysRevLett.129.236601](https://doi.org/10.1103/PhysRevLett.129.236601)

Intrinsic anisotropy is one of the most important questions to be addressed in diverse scientific disciplines including topological and correlated electron nanotechnology [1–7]. Strong electronic correlations and topology with strong spin-orbit coupling are widely recognized as fundamental sources of novel states of matter and technologically important material properties [8–14]. Topological Hall effect (THE) and angular magnetoresistance are quintessential embodiments of this concept. Moreover, skyrmion spin textures with a local spin chirality will induce a Berry phase to the wave function of conduction electrons and then make additional contribution to the Hall resistivity ρ_{xy} [15–18]. Since this additional contribution to the Hall effect originates from the topological spin texture, the term topological Hall effect is coined. THE has been observed in metallic skyrmion-hosting materials which show noncollinear ferromagnetic spin structure [19–21]. On the other hand, anisotropic magnetoresistance (AMR) in ferromagnets depends on the orientation of the magnetization with respect to the electric current direction in the material. It is sensitive to electronic structure, frustrated interactions, spin-orbit coupling, and magnetocrystalline anisotropy that also affect magnetic domain structure and consequently skyrmionic bubbles [22–27]. Although AMR and THE are rather important to assess the potential applications of skyrmions as information carriers in magnetic information storage and processing devices, the understanding of their microscopic mechanism and underlying anisotropy related to spin-orbit coupling is still poor.

The kagome structure is a hexagonal mesh lattice which is named after the traditional Japanese woven bamboo pattern. Materials with a kagome structure exhibit many

exotic physical properties such as quantum spin liquid, topological insulating states, Dirac or Weyl fermions, and magnetic skyrmions [25,28–31]. In particular, for the geometrically frustrated kagome bilayer metallic Fe₃Sn₂ magnet, a large anomalous Hall effect (AHE) and massive Dirac fermions have been reported [32,33]. In addition, recent studies on Fe₃Sn₂ have confirmed that topological spin textures exist over wide temperature and magnetic field (*T* – *B*) regions and a many-body spin-orbit tunability emerges at low temperature [25,34,35]. Stable skyrmionic spin textures in Fe₃Sn₂ appear at room temperature and can be manipulated by confinement in real devices [26,27,34,36–38], which is of considerable importance. Whereas Hall effect and its possible topological contribution have been investigated before in bulk crystals of Fe₃Sn₂ [32,39–41], such studies have all been undertaken for the in-plane current flow and magnetic field applied along the *c* axis.

In this Letter, we have studied interlayer transport by using focused ion beam (FIB) nanofabrication for the precise current path along the *c* axis and in the hexagonal plane of micron-size Fe₃Sn₂, commonly used in applications [26,27]. We not only delineate anisotropy of the Hall tensor by directional transport, but we also show for the first time the existence of THE and skyrmion bubbles when the magnetic field is applied in the hexagonal plane for the out-of-plane direction of current. Surprisingly, large THE is observed in the temperature region where magnetic skyrmions form, as well as at lower temperature where geometrically frustrated magnet enters the spin-glass state. Then, for the in-plane magnetic field direction, we present indirect insight into magnetocrystalline anisotropy and

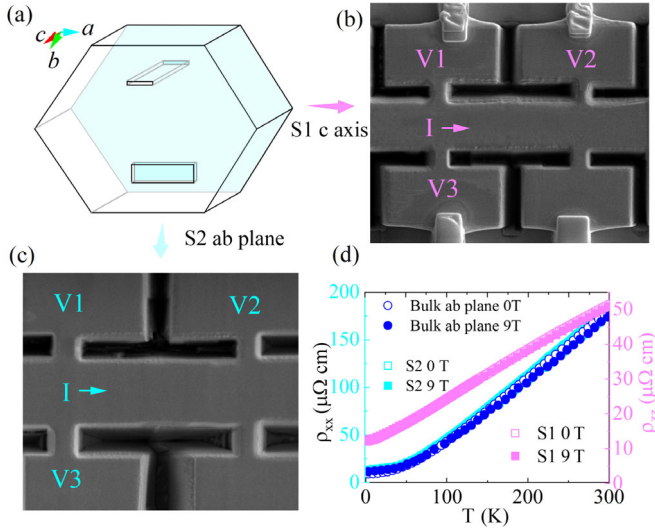


FIG. 1. The construction and photos of Hall bars for the current flows both along the c axis (S1) and in plane (S2) (a)–(c). I is the direction of electrical current, and V1, V2, and V3 are leads for voltage measurement. (d) Resistivity for both samples. We show bulk ab plane resistivity for comparison.

exchange interactions via angular magnetoresistance. We observe a fourfold AMR in a wide temperature and field range. The evolution of fourfold to twofold AMR [42–46] is consistent with the spin reorientation due to magnetic anisotropy and the competition of magnetic interactions.

As the crystal surface is vertical to the c axis [47–50], the FIB system is used for preparing Hall bars with long sides along in-plane and out-of-plane direction, as shown in Figs. 1(a)–1(c). The sample with out-of-plane long side is labeled S1 for current path along the c axis and the sample with long in-plane direction is S2 for current path in the ab plane. The longitudinal resistance measured as $R_{xx} = (V_1 - V_2)/I$ and Hall resistance measured as $R_{xy} = (V_3 - V_1)/I$ are converted to resistivity using $\rho = RA/l$, where A is a cross section and l is a current path distance. The Hall and magnetoresistance of S1 are ρ_{zy} and ρ_{xx} , respectively, as shown in Figs. 1(a)–1(c). For consistency and in order to avoid confusion, we use ρ_{xx} and ρ_{xy} to denote the magnetoresistance and Hall effect for both S1 and S2 in the text. Figure 1(d) shows the longitudinal resistivity under 0 and 9 T fields for both samples. Both samples show good metallic resistivity.

Figures 2(a), 2(c), and 2(e) show measurements relevant to sample S1. Figure 2(a) is the magnetization (M), measured on a crystal before device fabrication, with the magnetic field B parallel to the ab plane, which is the same magnetic field direction applied to sample S1 during current flows [Fig. 1(b)]. Figures 2(c) and 2(e) are measurement on S1 and show the magnetic field dependence at several temperatures of the magnetoresistance (MR) and the Hall resistivity, respectively. MR is defined as $[\rho_{xx}(B) - \rho_{xx}(0)]/\rho_{xx}(0) \times 100$. Figures 2(b), 2(d), and 2(f)

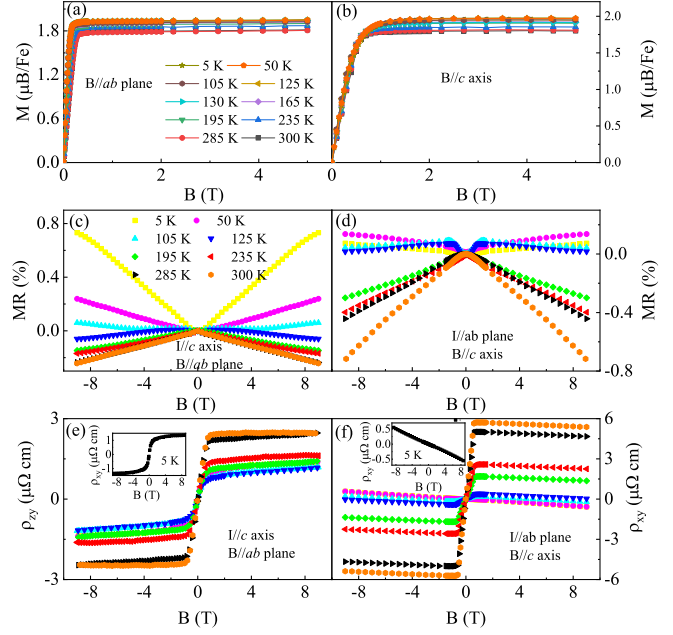


FIG. 2. Magnetization versus B for crystal before nanofabrication for magnetic field $B//ab$ plane (a) and $B//c$ axis (b). MR and ρ_{xy} versus B for sample S1 and S2 (c)–(f). Insets in (e),(f) show enlarged 5 K data. Panels (a),(b) and (c)–(f) use the same legend, respectively.

are the equivalent images to the ones in the left-hand column, but applied to S2 where current path is confined by FIB in the hexagonal plane. The data of S2 are consistent with the reported measurements where the current was flowing in the ab plane of bulk crystal [32]. For both S1 and S2, the magnetization saturates at relatively low field. In a magnetic material, the total Hall resistivity is described as the sum of three terms:

$$\begin{aligned} \rho_{xy} &= \rho_{xy}^N + \rho_{xy}^A + \rho_{xy}^T \\ &= R_0 B + S_H \rho^2 M + \rho_{xy}^T, \end{aligned} \quad (1)$$

where ρ_{xy}^N is the normal Hall resistivity due to the Lorentz force and R_0 is the ordinary Hall coefficient [18,51]. ρ_{xy}^A is the anomalous Hall resistivity which gives rise to the anomalous Hall effect that contains both an intrinsic Berry phase-related contribution and an extrinsic side jump and skew scattering-related contribution. For the intrinsic AHE, S_H is a constant because intrinsic anomalous Hall conductivity is linearly proportional to M [18,47,52]. The last term ρ_{xy}^T is the topological Hall resistivity from the noncollinear spin texture with nonzero scalar spin chirality [15–18].

R_0 derived from S1 is positive, indicating dominant holelike carriers for the out-of-plane conduction. This is opposite to the results of S2 where R_0 is negative indicating electron-type carriers, in agreement with a previous report [32]. The apparent carrier density n_0 calculated from R_0 is

shown in Fig. 3(a). Opposite signs for in-plane and out-of-plane carriers indicate strong anisotropy in the electronic structure. Both S_H for S1 and S2 are positive [Fig. 3(b)]. The former is about 5 times that of the latter at $T > 100$ K. Its absolute value is comparable with those in typical ferromagnetic (FM) materials and other kagome metals, such as Fe (0.06 V^{-1}), MnSi (-0.19 V^{-1}), Mn_3Sn ($0.07\text{--}0.24 \text{ V}^{-1}$), YMn_6Sn_6 ($0.04\text{--}0.07 \text{ V}^{-1}$), and $\text{Co}_3\text{Sn}_2\text{S}_2$ (0.05 V^{-1}) [53–56]. In our measurements, the in-plane Hall resistivity (S2) shows almost no AHE at low temperature [47] while the AHE not only exists in out-of-plane measurements at low temperature, but also gives a large S_H around 1 V^{-1} [Fig. 3(b) [47]].

ρ_{xy}^T is estimated by subtracting ρ_{xy}^N and ρ_{xy}^A [47]. As shown in Figs. 3(c) and 3(d), ρ_{xy}^T has nonzero values only at low field regime for both samples. When the field is high, which leads to a fully polarized state, ρ_{xy}^T vanishes and the other two terms dominate. In low magnetic fields, at temperature higher than 100 K, the absolute value of ρ_{xy}^T increases with increasing temperature, reaching the maximum values of $\rho_{xy,S1}^{T,\max} = -1.35 \mu\Omega \text{ cm}$ and $\rho_{xy,S2}^{T,\max} = -0.54 \mu\Omega \text{ cm}$. The maximum value for S2 is consistent with a former report, but the behavior differs from the report above $T = 200$ K. $\rho_{xy,S2}^T$ shows another positive peak to the right of the negative peak with a maximum positive intensity of $0.24 \mu\Omega \text{ cm}$ at 300 K [40]. The difference of critical B values with the former report may come from the reduced sample size. This suggests the THE in Fe_3Sn_2 sample S2 for B along the c axis may come from both a topological nontrivial state and noncollinear or noncoplanar spin configuration in real

space [57]. At lower temperature, $\rho_{xy,S2}^T$ disappears just like ρ_{xy}^A whereas $\rho_{xy,S1}^T$ for S1 still exhibits a peak value of $-0.77 \mu\Omega \text{ cm}$.

The relationship between field-induced magnetic structure and emergent anisotropy becomes clear if we compare the field range of nonzero ρ_{xy}^T [Figs. 3(e) and 3(f)] with the reported phase diagram where magnetic field $B//c$ [Fig. 3(f), open symbols] [25]. For $\rho_{xy,S1}^T$, the current is along the c axis and the field is inside the ab plane. When the temperature decreases below 100 K, the magnetic anisotropy for Fe_3Sn_2 changes its easy orientation direction from the c axis to the ab plane [58]. With increasing field and magnetic anisotropy, the spin glass is destroyed and this may lead to noncollinear or noncoplanar spin configuration which contributes to the THE. In the region above $T \approx 125$ K, ρ_{xy}^T only shows large values in the bubble or skyrmion bubble phases where topologically nontrivial magnetic structures with large spin chirality exist. In Fig. 3(e), the contour plots show a clear boundary (yellow area). As the magnetic phase diagram for $B//ab$ is hitherto unknown, our results show possible areas where topological nontrivial phases may exist. For $\rho_{xy,S2}^T$, the negative peak is in the bubble phase while the positive peak is in the skyrmion bubble phase.

In order to study the spin reorientation and possible topological nontrivial spin structure in S1, which will give an intuitive understanding of the THE, we show the Lorentz transmission electron microscopy images taken at 300 and 104 K in Figs. 3(g) and 3(h), respectively. Based on the electron diffraction patterns [47], the c axis is indicated in the images. At 300 K [Fig. 3(g)], stripe domains with spin

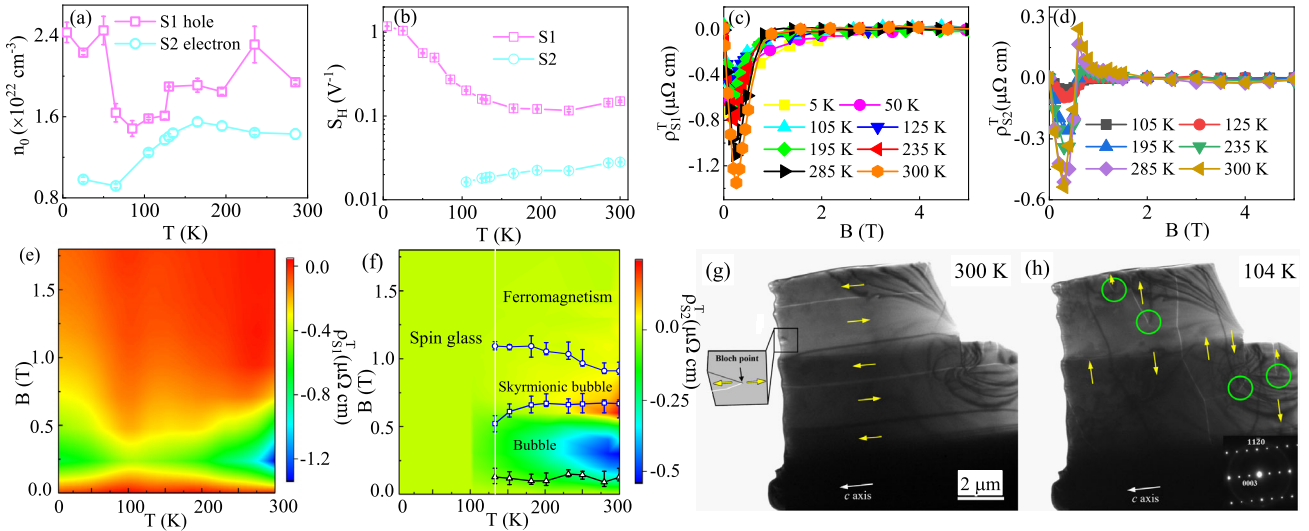


FIG. 3. Temperature dependence of (a) the apparent carrier density and (b) S_H for both samples. Panels (c) and (d) show ρ_{xy}^T as function of B at selected temperatures for sample S1 and S2, respectively. The contour plots correspond to (e) $\rho_{xy,S1}^T(T, B)$ and (f) $\rho_{xy,S2}^T(T, B)$ for T between 5 and 300 K and B from 0 to 1.8 T. The open symbols represent critical fields of different magnetic phases from Ref. [25]. The field direction of the regenerated phase diagram is $B//c$. Color intensity maps show results in this Letter. Panels (g) and (h) show Lorentz transmission electron microscopy images taken at 300 and 104 K, respectively, with defocus value $+576 \mu\text{m}$. The inset in (g) shows the spin configuration.

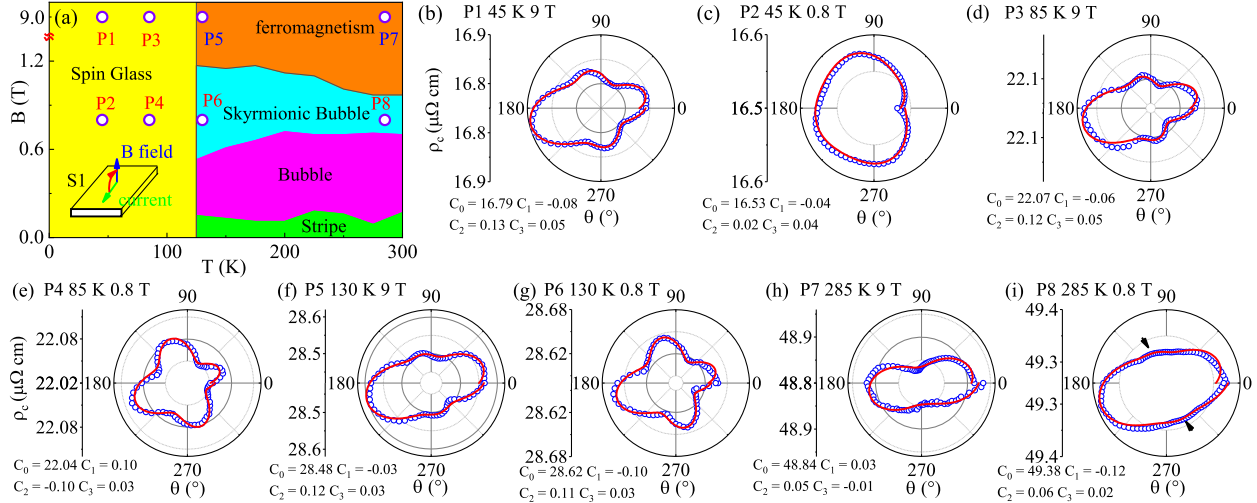


FIG. 4. (a) B - T phase diagram of Fe_3Sn_2 regenerated from Ref. [25]. The positions of P1–P8 are shown by open circle symbols. The inset shows the relation between the current and field. The green arrow is the current direction and the blue arrow is the field. The red arrow indicates the rotation direction. Panels (b)–(i) show AMR results for P1–P8. The open blue symbols are measured data and the red lines are fitting as Eq. (3). The fitting parameters are listed in the left-hand corner of each panel. The black arrows in (i) indicate the weak fourfold behavior in P8.

directions along the c axis are separated by either bright or dark lines. Yellow arrows indicate spin directions for domains. The bright and dark lines are domain walls with the out-of-plane spins (spin directions are in the imaging direction). At the sample edge, the small triangular domain indicated with a rectangle in Fig. 3(g) can be considered as a precursor of a skyrmionic bubble when viewed along the c axis. Upon cooling to 104 K, the domain walls rotate about 90° without changing the domain wall contrast (bright or dark). In addition, the triangular bubbles are rotated by 90° , indicated with green circles. The 90° rotation of domain walls and bubbles indicates a clear 90° spin reorientation transition. The spin reorientation occurs in the range of temperature from 170 to 110 K upon cooling. In this TEM sample, the spin reorients from the c axis to the $[11\bar{2}0]$ direction (an in-plane direction in thin TEM lamella). As a result, the skyrmionic bubbles in the ab plane at room temperature will be destabilized across the 90° spin reorientation transition, consistent with our THE measurements. Skyrmionic bubbles may form in the plane perpendicular to the c axis below the 90° spin reorientation transition. We note that the triangular domain [Fig. 3(g) inset] has a singular Bloch point where two antiparallel domains and two side domain walls meet. This spin configuration is similar to the chiral bobber structures in FeGe [59], coexisting with skyrmion phases over large magnetic field and temperature range.

For insight into the contributions of magnetic interactions to electronic transport, we studied the AMR for sample S1 (Fig. 4). The relationship between current, magnetic field, and rotation direction is shown in Fig. 4(a). When the field is perpendicular to the current, θ is 0° . Figure 4(a) is a magnetic phase diagram from Ref. [25]. We selected eight points

P1–P8 at different magnetic phases, and the AMR results for these points are shown in Figs. 4(b)–4(i). A fourfold AMR is clearly revealed at several points. There is asymmetry; i.e., the values at 0° and 360° are different from 180° at low temperature which may come from the magnetic anisotropy [47]. The AMR in cubic crystals can be fitted by a phenomenological model [23,60]:

$$\rho_{xx}(\theta) = C_0 + C_1 \cos^2 \theta + C_2 \cos^4 \theta. \quad (2)$$

In order to introduce the magnetic anisotropy and fit the observed data, we add another phenomenological term into this model:

$$\rho_{xx}(\theta) = C_0 + C_1 \cos^2 \theta + C_2 \cos^4 \theta + C_3 \sin^2 \theta. \quad (3)$$

As the AMR depends on the orientation of the magnetization with respect to the electric current direction, it is important to confirm the magnetic ground state of the system [61]. The ground state of the Fe_3Sn_2 honeycomb lattice is determined by the relation between competition of ferromagnetic and antiferromagnetic (AFM) exchange interactions and magnetic anisotropy which may come from Kitaev-type interactions [62]. Magnetic anisotropy changes with temperature and there is a spin glass to FM state or skyrmionic state transition, where both magnetic interactions competition and exchange anisotropy exist. That could explain the evolution of AMR behavior. Both P1 and P2 points are in the spin glass state where the competition of exchange interactions is strong and there is an easy-plane (ab -plane) anisotropy. With increasing field from P2 (0.8 T) to P1 (9 T), when the external magnetic field is strong enough to overcome the magnetocrystalline

anisotropy field, the spin distribution should be completely determined by the field direction which favors FM spin configuration. This is equivalent to increasing the ratio factor α that measures the relative magnitude of FM and AFM exchanges, with fixed anisotropy factor μ that measures the Kitaev exchange anisotropy along the c axis; see Ref. [47]. Hence, the ground state changes from a twofold to a fourfold state. When temperature increases from P2 (45 K) to P4 (85 K), the spin rotates from inside the ab plane to along the c axis and the peak of the change occurs at ≈ 120 K around P6. Then the twofold to fourfold AMR [black arrows in Fig. 4(i)] evolution could be explained by the increasing magnetic anisotropy in P7 and P8, respectively. Figure S4 in Ref. [47] shows the approximate evolution of exchange interactions competition and magnetic anisotropy among the eight selected points.

In summary, we present a comprehensive study of electronic transport anisotropy in micron-size Fe_3Sn_2 crystals with emphasis on hitherto unknown kagome interlayer transport for current path along the c axis. Different from the in-plane transverse resistivity, the out-of-plane Hall effect shows both AHE and THE at even lower temperature where the system enters the spin-glass state. These findings indicate that the kagome magnetic metals show unique anisotropic topological features not only in momentum space but also in real space. Moreover, the AMR where current path is confined along the c axis shows fourfold symmetry and evolution between fourfold and twofold symmetry which could be explained by the competing interactions within the exchange-anisotropic Kitaev-Heisenberg model [62]. Our results deepen the understanding of the asymmetric magnetic interaction and topological chirality on the topological Hall component in mesoscopic crystals which is important in future functional device design.

Work at BNL is supported by the Office of Basic Energy Sciences, Materials Sciences and Engineering Division, U.S. DOE under Contract No. DE-SC0012704. This research also used resources of the Center for Functional Nanomaterials (CFN), which is a U.S. Department of Energy Office of Science User Facility, at Brookhaven National Laboratory under Contract No. DE-SC0012704.

*These authors contributed equally to this work.

[†]Present address: Material Science Division, Argonne National Laboratory, Lemont, Illinois 60439, USA.

[‡]qdu@anl.gov

[§]petrovic@bnl.gov

- [1] J. S. Gallagher III and F. Halzen, *Science* **357**, 1240 (2017).
 [2] Y. He *et al.*, *Adv. Mater.* **32**, 2004331 (2020).
 [3] M. Rauzi, P. Verant, T. Lecuit, and P.-F. Lenne, *Nat. Cell Biol.* **10**, 1401 (2008).
 [4] I. C. McManus, *Nature (London)* **259**, 426 (1976).
 [5] A. A. Khajetoorians and J. Wiebe, *Science* **344**, 976 (2014).
 [6] J. C. Oberg, M. R. Calvo, F. Delgado, M. M. Lagares, D. Serrate, D. Jacob, J. Fernandez-Rossier, and C. F. Hirjibehedin, *Nat. Nanotechnol.* **59**, 261 (2010).
 [7] Y. Yan, X. Zhou, H. Jin, C.-Z. Li, X. Ke, G. V. Tendeloo, K. Liu, D. Yu, M. Dressel, and Z.-M. Liao, *ACS Nano* **9**, 10244 (2015).
 [8] D. S. L. Abergel, V. Apalkov, J. Berashevich, K. Ziegler, and T. Chakraborty, *Adv. Phys.* **59**, 261 (2010).
 [9] X. Wan, A. M. Turner, A. Vishwanath, and S. Y. Savrasov, *Phys. Rev. B* **83**, 205101 (2011).
 [10] B.-J. Yang, E.-G. Moon, H. Isobe, and N. Nagaosa, *Nat. Phys.* **10**, 774 (2014).
 [11] S. A. Yang, H. Pan, and F. Zhang, *Phys. Rev. Lett.* **113**, 046401 (2014).
 [12] H. Wei, S.-P. Chao, and V. Aji, *Phys. Rev. B* **89**, 235109 (2014).
 [13] S. D. Huber, *Nat. Phys.* **12**, 621 (2016).
 [14] C. Beenakker and L. Kouwenhoven, *Nat. Phys.* **12**, 618 (2016).
 [15] P. Bruno, V. K. Dugaev, and M. Taillefumier, *Phys. Rev. Lett.* **93**, 096806 (2004).
 [16] K. Ueda, S. Iguchi, T. Suzuki, S. Ishiwata, Y. Taguchi, and Y. Tokura, *Phys. Rev. Lett.* **108**, 156601 (2012).
 [17] B. G. Ueland, C. F. Miclea, Y. Kato, O. Ayala-Valenzuela, R. D. McDonald, R. Okazaki, P. H. Tobash, M. A. Torrez, F. Ronning, R. Movshovich, Z. Fisk, E. D. Bauer, I. Martin, and J. D. Thompson, *Nat. Commun.* **3**, 1067 (2012).
 [18] N. Nagaosa, J. Sinova, S. Onoda, A. H. MacDonald, and N. P. Ong, *Rev. Mod. Phys.* **82**, 1539 (2010).
 [19] A. Neubauer, C. Pfleiderer, B. Binz, A. Rosch, R. Ritz, P. G. Niklowitz, and P. Böni, *Phys. Rev. Lett.* **102**, 186602 (2009).
 [20] N. Kanazawa, Y. Onose, T. Arima, D. Okuyama, K. Ohoyama, S. Wakimoto, K. Kakurai, S. Ishiwata, and Y. Tokura, *Phys. Rev. Lett.* **106**, 156603 (2011).
 [21] T. Yokouchi, N. Kanazawa, A. Tsukazaki, Y. Kozuka, M. Kawasaki, M. Ichikawa, F. Kagawa, and Y. Tokura, *Phys. Rev. B* **89**, 064416 (2014).
 [22] J. Smit, *Physica* **17**, 612 (1951).
 [23] T. McGuire and R. Potter, *IEEE Trans. Magn.* **11**, 1018 (1975).
 [24] R. I. Potter, *Phys. Rev. B* **10**, 4626 (1974).
 [25] Z. Hou, W. Ren, B. Ding, G. Xu, Y. Wang, B. Yang, Q. Zhang, Y. Zhang, E. Liu, F. Xu, W. Wang, G. Wu, X. Zhang, B. Shen, and Z. Zhang, *Adv. Mater.* **29**, 1701144 (2017).
 [26] Z. Hou, Q. Zhang, X. Zhang, G. Xu, J. Xia, B. Ding, H. Li, S. Zhang, N. M. Batra, P. M. F. J. Costa, E. Liu, G. Wu, M. Ezawa, X. Liu, Y. Zhou, X. Zhang, and W. Wang, *Adv. Mater.* **32**, 1904815 (2020).
 [27] Z. Hou, Q. Zhang, G. Xu, S. Zhang, C. Gong, B. Ding, H. Li, F. Xu, Y. Yao, E. Liu, G. Wu, X.-x. Zhang, and W. Wang, *ACS Nano* **13**, 922 (2019).
 [28] S. Yan, D. A. Huse, and S. R. White, *Science* **332**, 1173 (2011).
 [29] Z. Liu, E. J. Bergholtz, H. Fan, and A. M. Läuchli, *Phys. Rev. Lett.* **109**, 186805 (2012).
 [30] I. I. Mazin, H. O. Jeschke, F. Lechermann, H. Lee, M. Fink, R. Thomale, and R. Valentí, *Nat. Commun.* **5**, 4261 (2014).
 [31] K. Kuroda *et al.*, *Nat. Mater.* **16**, 1090 (2017).

- [32] Q. Wang, S. Sun, X. Zhang, F. Pang, and H. Lei, *Phys. Rev. B* **94**, 075135 (2016).
- [33] L. Ye, M. Kang, J. Liu, F. V. Cube, C. R. Wicker, T. Suzuki, C. Jozwiak, A. Bostwick, E. Rotenberg, D. C. Bell, L. Fu, R. Comin, and J. G. Checkelsky, *Nature (London)* **555**, 638 (2018).
- [34] Z. Hou, Q. Zhang, G. Xu, C. Gong, B. Ding, Y. Wang, H. Li, E. Liu, F. Xu, H. Zhang, Y. Yao, G. Wu, X.-x. Zhang, and W. Wang, *Nano Lett.* **18**, 1274 (2018).
- [35] J.-X. Yin, S. S. Zhang, H. Li, K. Jiang, G. Chang, B. Zhang, B. Lian, C. Xiang, I. Belopolski, H. Zheng, T. Cochran, S. Xu, G. Bian, K. Liu, T. Chang, H. Lin, Z. Lu, Z. Wang, S. Jia, W. Wang, and M. Hasan, *Nature (London)* **562**, 91 (2018).
- [36] J. Tang, L. Kong, Y. Wu, W. Wang, Y. Chen, Y. Wang, J. Li, Y. Soh, Y. Xiong, M. Tian, and H. Du, *ACS Nano* **14**, 10986 (2020).
- [37] B. Wang, P.-k. Wu, N. Bagués Salguero, Q. Zheng, J. Yan, M. Randeria, and D. W. McComb, *ACS Nano* **15**, 13495 (2021).
- [38] W. Wei, J. Tang, Y. Wu, Y. Wang, J. Jiang, J. Li, Y. Soh, Y. Xiong, M. Tian, and H. Du, *Adv. Mater.* **33**, 2101610 (2021).
- [39] C. D. O'Neill, A. S. Wills, and A. D. Huxley, *Phys. Rev. B* **100**, 174420 (2019).
- [40] H. Li, B. Ding, J. Chen, Z. Li, Z. Hou, E. Liu, H. Zhang, X. Xi, G. Wu, and W. Wang, *Appl. Phys. Lett.* **114**, 192408 (2019).
- [41] H. Li, B. Zhang, J. Liang, B. Ding, J. Chen, J. Shen, Z. Li, E. Liu, X. Xi, G. Wu, Y. Yao, H. Yang, and W. Wang, *Phys. Rev. B* **101**, 140409(R) (2020).
- [42] C. Wang, H. Seinige, G. Cao, J.-S. Zhou, J. B. Goodenough, and M. Tsoi, *Phys. Rev. X* **4**, 041034 (2014).
- [43] P. Li, C. Jin, E. Y. Jiang, and H. L. Bai, *J. Appl. Phys.* **108**, 093921 (2010).
- [44] C. R. Hu, J. Zhu, G. Chen, J. X. Li, and Y. Z. Wu, *arXiv*: 1105.5781.
- [45] N. Kumar, N. Wadehra, R. Tomar, Shama, S. Kumar, Y. Singh, S. Dattagupta, and S. Chakraverty, *Adv. Quantum Technol.* **4**, 2000081 (2021).
- [46] Y. Dai, Y. W. Zhao, L. Ma, M. Tang, X. P. Qiu, Y. Liu, Z. Yuan, and S. M. Zhou, *Phys. Rev. Lett.* **128**, 247202 (2022).
- [47] See Supplemental Material at <http://link.aps.org/supplemental/10.1103/PhysRevLett.129.236601> for experimental details, calculation of AHE, anisotropic magnetoresistance details, discussion of the ground state of the honeycomb lattice and Lorentz TEM.
- [48] Z. Fisk and J. Remeika, in *Handbook on the Physics and Chemistry of Rare Earths*, edited in K. A. Gschneidner, Jr. and L. Eyring (Elsevier Science B.V., 2009), Vol. 12, p. 53.
- [49] Q. Du, M.-G. Han, Y. Liu, W. Ren, Y. Zhu, and C. Petrovic, *Adv. Quantum Technol.* **3**, 2000058 (2020).
- [50] B. Malaman, B. Roques, A. Courtois, and J. Protas, *Acta Crystallogr. Sect. B* **32**, 1348 (1976).
- [51] N. Nagaosa and Y. Tokura, *Nat. Nanotechnol.* **8**, 899 (2013).
- [52] C. Zeng, Y. Yao, Q. Niu, and H. H. Weitering, *Phys. Rev. Lett.* **96**, 037204 (2006).
- [53] S. Nakatsuji, N. Kiyohara, and T. Higo, *Nature (London)* **527**, 212 (2015).
- [54] Q. Wang, Y. Xu, R. Lou, Z. Liu, M. Li, Y. Huang, D. Shen, H. Weng, S. Wang, and H. Lei, *Nat. Commun.* **9**, 1 (2018).
- [55] P. Dheer, *Phys. Rev.* **156**, 637 (1967).
- [56] A. Neubauer, C. Pfleiderer, R. Ritz, P. Niklowitz, and P. Böni, *Physica (Amsterdam)* **404B**, 3163 (2009).
- [57] Y. He, S. Schneider, T. Helm, J. Gayles, D. Wolf, I. Soldatov, H. Borrmann, W. Schnelle, R. Schaefer, G. H. Fecher, B. Rellinghaus, and C. Felser, *Acta Mater.* **226**, 117619 (2022).
- [58] A. Biswas, O. Iakutkina, Q. Wang, H. C. Lei, M. Dressel, and E. Uykur, *Phys. Rev. Lett.* **125**, 076403 (2020).
- [59] Z. Fengshan, F. N. Rybakov, B. A. B., S. Dongsheng, W. Shasha, L. Z.-A. nand Du Haifeng, K. N. S., C. Jan, K. Andras, T. Mingling, Z. Yuheng, B. Stefan, and D.-B. R. E., *Nat. Nanotechnol.* **13**, 451 (2018).
- [60] R. Ramos, S. K. Arora, and I. V. Shvets, *Phys. Rev. B* **78**, 214402 (2008).
- [61] N. Kumar, Y. Soh, Y. Wang, and Y. Xiong, *Phys. Rev. B* **100**, 214420 (2019).
- [62] X. M. Zhang, R. M. Liu, Z. Jin, T. T. Liu, D. Y. Chen, Z. Fan, M. Zeng, X. B. Lu, X. S. Gao, M. H. Qin, and J.-M. Liu, *Phys. Rev. E* **102**, 042132 (2020).